OPEN

Atomic configurations at InAs partial dislocation cores associated with Z-shape faulted dipoles

Luying Li[1,2], Zhaofeng Gan[2], Martha R. McCartney[2], Hanshuang Liang[3], Hongbin Yu[3], Yihua Gao[1,4], Jianbo Wang[5] & David J. Smith[2]

[1]Center for Nanoscale Characterization and Devices, Wuhan National Laboratory for Optoelectronics, Huazhong University of Science and Technology, Wuhan 430074, China, [2]Department of Physics, Arizona State University, Tempe, Arizona 85287, USA, [3]School of Electrical, Computer, and Energy Engineering, Arizona State University, Tempe, Arizona 85287, USA, [4]School of Physics, Huazhong University of Science and Technology, Wuhan, 430074, China, [5]School of Physics and Technology, Center for Electron Microscopy and MOE Key Laboratory of Artificial Micro- and Nano-Structures, Wuhan University, Wuhan 430072, China.

The atomic arrangements of two types of InAs dislocation cores associated by a Z-shape faulted dipole are observed directly by aberration-corrected high-angle annular-dark-field imaging. Single unpaired columns of different atoms in a matrix of dumbbells are clearly resolved, with observable variations of bonding lengths due to excess Coulomb force from bare ions at the dislocation core. The corresponding geometric phase analysis provides confirmation that the dislocation cores serve as origins of strain field inversion while stacking faults maintain the existing strain status.

Polytype superlattices consisting of chemically identical but structurally different materials have attracted intense study in recent years, both for controlled growth of twinning and polytypic superlattices in nanostructural materials[1–4], and for exploring possible electronic and optoelectronic applications[5–8]. Because of the low stacking fault energy of cubic III-V compound semiconductors[9], it is relatively easy to produce stacking faults on {111} planes, which then facilitate the formation of parallel twins and polytypic superlattices. Under certain conditions, twins and stacking faults on different {111} planes intersect and form different types of dislocation cores. Knowledge of the dislocation core structure can play a vital role in explaining the electronic and dynamical properties of defects in semiconductors. In this study, the atomic structures of two InAs dislocation cores, associated by a Z-shape faulted dipole, are directly observed, and single columns of unpaired atoms embedded in a matrix of atomic dumbbells are clearly resolved using aberration-corrected high-angular-dark-field (HAADF) imaging. Experimental measurement of the strain fields around the two dislocation cores are obtained based on geometric phase analysis (GPA).

Aberration-corrected HAADF imaging is a very powerful technique for determining structural as well as chemical information at atomic resolution. It has been applied, for example, to segregation and dislocation in a Ga-terminated 30° partial dislocation core in GaAs[10], antisite defects in LiFePO$_4$[11], the chemical identity of individual atoms in hexagonal BN monolayers that contain substitutional defects[12], and the interfaces of InGaAs-InAlAs superlattices[13]. A recent paper describes applications to studying dislocation core structures in CdTe solar-cell material[14]. The utilization of aberration-corrected HAADF imaging in the current study has made it possible to determine the atomic structure of a Z-shape faulted dipole within the central area of an InAs nanopillar, that is comparatively thick (thickness of $\sim$ 70 nm according to electron holography measurement). The overall structural features of the faulted dipole as well as atomic arrangements at the dislocation core were simultaneously obtained, and variations of bond length for pairs of atomic columns ("dumbbells") close to the dislocation cores were also determined.

The Z-shape faulted dipole was first reported by Mader as faint straight lines along <110> directions in strong-beam electron micrographs of deformed f.c.c. metals[15]. This defect was suggested by Hirsch to be a long Frank loop[16], and it was later discussed in detail by Seeger who proposed that the Frank dislocations were dissociated on the primary glide plane[17]. The Z-shape faulted dipole includes three stacking faults and four partial dislocations (i.e., two stair rods and two Shockley partials). The determination of stacking fault energy from the faulted dipole geometry using lattice imaging was reported[18–19], and the atomic structure of the central
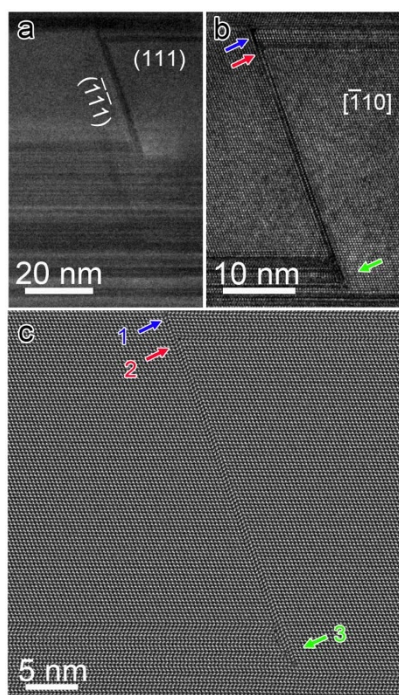
Figure 1 | Overall features of a Z-shape faulted dipole. (a) TEM image of a Z-shape faulted dipole in InAs nanopillar. (b) HREM image of the faulted dipole projected along the [$\bar{1}$10] direction showing rotational twins and stacking faults intersecting at 70.5°. Dislocation cores are indicated by blue, red and green arrows. (c) Aberration-corrected HAADF image of the faulted dipole with atomic dumbbells of the lattices and stacking sequences of the stacking faults clearly resolved. The dislocation cores are labeled with colored arrows similar to (b).

stacking faults of a Z-shape faulted dipole in deformed GaAs was determined based on HREM imaging and image simulations[20].

Results

The conventional TEM image in Fig. 1a shows many parallel dark lines perpendicular to [111] direction intersecting the other dark line perpendicular to [$\bar{1}\bar{1}$1] direction at 70.5°, forming the so-called Z-shape faulted dipole. Fig. 1b is an HREM image projected along [$\bar{1}$10] direction which indicates that the dark lines correspond to rotational twins and stacking faults. Since the twins and stacking faults which lie on (111) planes extend to the nanopillar surfaces, there are no partial dislocations at the far ends of the faulted dipole. Several stair-rod dislocations are pinned along the stacking faults on ($\bar{1}\bar{1}$1) planes, which is different from the classic Z-shape faulted dipole. Due to limited resolution (point resolution: 0.19 nm) of the microscope used for imaging, the atomic dumbbells of the lattice can not be resolved (dumbbell of InAs crystal: 0.15 nm), and the stacking sequences of the stacking faults and atomic arrangements at the dislocation cores are not clear due to local strain as well as some image delocalization that occurs in a microscope without aberration correction. Fig. 1c is an aberration-corrected HAADF image with hardly any diffraction contrast and delocalization: the atomic dumbbells of the crystal lattice and stacking sequences of the stacking faults are clearly resolved. The two dislocation cores indicated by blue and red arrows are discussed in more detail below based on aberration-corrected HAADF images recorded at higher magnification.

It is well known that the scanning transmission electron microscopy (STEM) scanning system and the CCD camera often have distortions that affect the images formed[21]. The shear distortions present in the aberration-corrected HAADF image in Fig. 2a have been removed, according to the perfect zincblende structure in [$\bar{1}$10]

projection. In order to check to what extent the obtained image might have been affected by environmental instabilities, the Jitterbug software was applied to the image[22]. However, it was found that the resulting STEM-HAADF image was almost unchanged from the original, which indicated that it was recorded under conditions of high instrumental stability.

The locations of two dislocation cores are indicated by blue (core 1) and red (core 2) arrows. Stacking sequence analysis reveals that core 1 is formed by the interaction of one intrinsic stacking fault and two growth twins with staggered twinning planes, while core 2 is at the intersection of one extrinsic stacking fault and one intrinsic stacking fault. The area contained in the white box including both dislocation cores is filtered using the annular mask tool in Digital Micrograph to remove high frequency noise, and presented in Fig. 2b at higher magnification. The cation and anion atomic columns are clearly resolved with one column having much brighter contrast than the other. Energy-dispersive X-ray spectra (EDS) from the dislocation core as well as from a region free of defects were obtained and overlapped (Fig. S1). Both spectra show no sign of Sb, and the corresponding In and As peaks are almost coincident, with just some peak intensities of In and As at the dislocation core being slightly lower. Thus, it could be concluded based on the EDS results that there is no accumulation of Sb dopants at the dislocation core or else trace amounts only. Considering the thickness of the material ($\sim$ 70 nm), the introduction of Sb would not be expected to have marked impact on the image intensity. Thus, for simplicity we have labeled the observed dumbbells as In-As with brighter image contrast corresponding to In^{3+} ($Z_{In} = 49$) and darker image contrast corresponding to As^{3-} ($Z_{As} = 33$).

Both dislocation cores are composed of two columns of single atoms and four columns of dumbbells, where three dumbbells point towards the core with light atoms and one with heavy atoms. The results of intensity line profiles across two atomic columns outside the defect, and two atomic columns at the dislocation cores, as labeled by the white dashed arrows in Fig. 2b, are presented in Figs. 2c and 2d, respectively. The profile of core 1 has two peaks with average intensity level of 2.4×10^5 and two of 1.5×10^5, while all four peaks in the line profile of core 2 have intensity level of 2.4×10^5. Thus, the two columns of single atoms in core 1 should be As^{3-}, while the two columns of single atoms in core 2 should be In^{3+}. Close inspection of the atomic structure of core 1 reveals that the In-As bonding lengths of the dumbbells closest to the single As^{3-} column are slightly shorter than normal (the average variation of In-As bonding length: $\Delta l \approx 0.05$ nm), as indicated by the black arrow heads in core 1, which could result from excess Coulomb repulsive force from the nearby single As^{3-} columns. On the other hand, the In^{3+} and As^{3-} atomic columns of the dumbbells closest to the single In^{3+} columns are clearly resolved, as indicated by the black arrow heads in core 2, even though the In-As bond lengths do not appear to be longer than normal. The error bar in the determination of the actual atomic positions is around 0.015 nm (see supplemental information for more details).

Atomic models for the regions outlined in white boxes in Fig. 2b are presented in Figs. 2e–2f: these are based on using the peak-finding algorithm to locate the atomic column positions and the relationship between intensity I and elemental number Z: $I \sim Z^n$ (where n is mainly determined by the geometry of the annular detection angles)[23]. The formation of core 1 can be attributed to the reaction of 30° Shockley partial dislocations bordering the stacking faults. Rotational twins with staggered twinning planes form a 30° Shockley partial dislocation with Burgers vector $\mathbf{b}_{11} = (a/6) [1\bar{2}1]$ (Cδ) lying in a (111) plane, which is indicated in Fig. 2e by a green triangle. This partial dislocation reacts with the other 30° partial with Burgers vector $\mathbf{b}_{12} = (a/6) [\bar{2}1\bar{1}]$ (αC) lying in a ($\bar{1}\bar{1}$1) plane indicated by an orange triangle. The overall Burgers vector of core 1 is obtained as: $\mathbf{b}_1 = \mathbf{b}_{11} + \mathbf{b}_{12} = (a/6) [\bar{1}\bar{1}0]$ ($\alpha\delta$), which is perpendicular to the
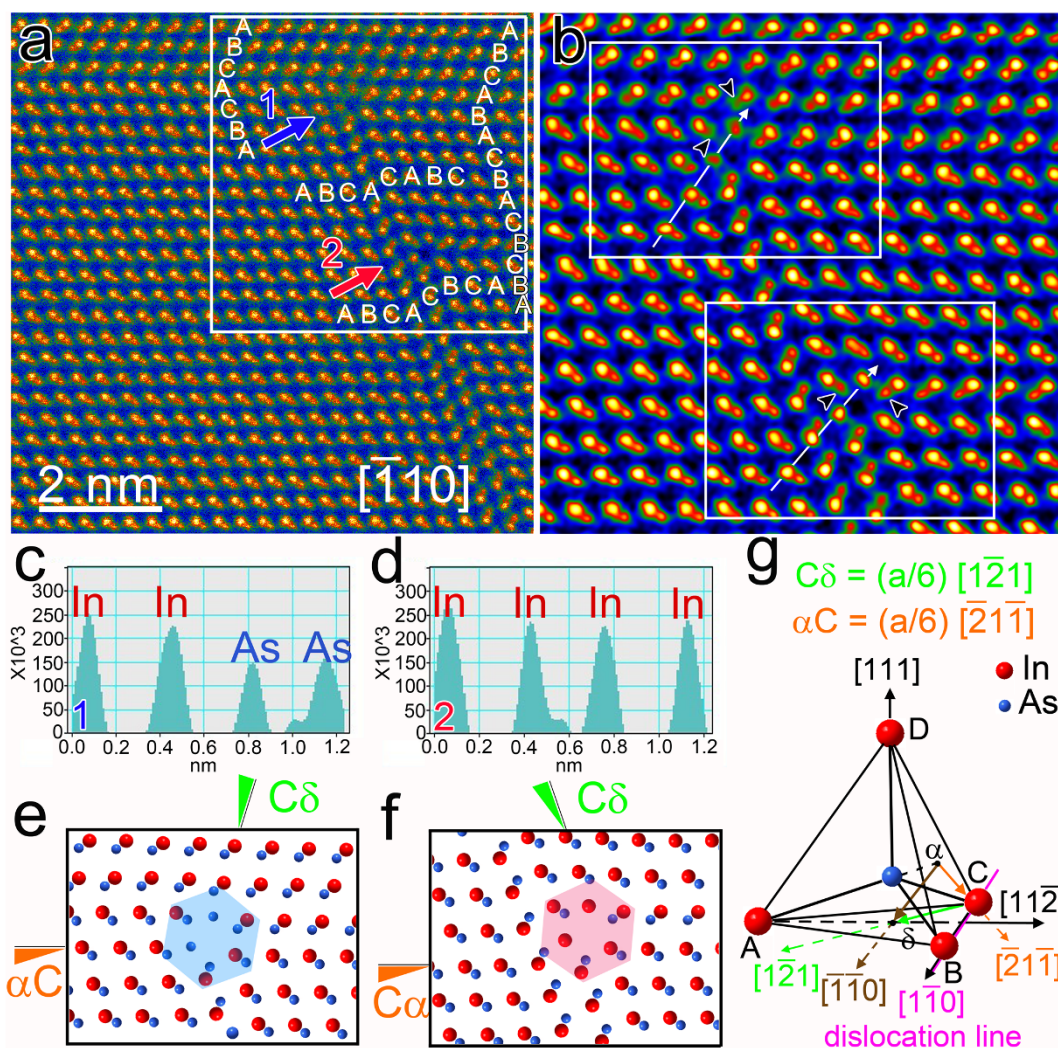
Figure 2 | Dislocation cores with opposite ions at atomic resolution. (a) Aberration-corrected HAADF image of dislocation cores 1 and 2 as projected along the [$\bar{1}$10] direction. The location of dislocation cores are indicated by blue and red arrows, and the corresponding stacking sequences are overlapped. (b) Area contained in the white box in (a) shown at higher magnification. The atomic arrangements at dislocation cores and stacking faults are clearly resolved. The dumbbells nearest to the single atomic columns at dislocation cores with bond length variations are indicated by black arrow heads. The intensity line profiles at dislocation cores are labeled by white dashed arrows and the results are presented in (c) and (d), respectively. (e) and (f) Corresponding atomic models of the two regions framed by white boxes in (b). (g) Sketch of geometric relationship of the Burgers vectors and the dislocation line according to Thompson's notation.

dislocation line in [1$\bar{1}$0] direction, and verifies the formation of an edge dislocation. The geometric relationship of the above Burgers vectors and the dislocation line are sketched in Fig. 2g according to Thompson's notation. The mechanism of dislocation formation for core 1 can be expressed as: $\alpha C + C\delta \rightarrow \alpha\delta$, which resembles part of the reported double-V shaped dislocation in diamond thin films, which has a core structure that is not as complex as this case[24].

The formation of core 2 can be explained as follows. The leading 30° partial dislocation $C\delta$, which is dissociated from a perfect 60° dislocation lying in a (111) plane, reacts with the stacking fault lying in a ($\bar{1}\bar{1}$1) plane. The incoming partial $C\delta$ would dissociate into a stair-rod $\alpha\delta$ and another partial dislocation $C\alpha$. While gliding on the ($\bar{1}\bar{1}$1) stacking-fault plane, the partial $C\alpha$ starts to transform the intrinsic stacking fault into an extrinsic stacking fault, and finally join the partials at the bottom end. Thus, the formation mechanism of core 2 could be expressed as: $C\delta \rightarrow C\alpha + \alpha\delta$, which has been discussed in detail as an example of the reaction between a dislocation and a stacking fault in nanocrystalline Al[25]. Our study provides direct experimental evidence for the theoretical study but with much more information about the dislocation core.

Non-stoichiometric dislocation cores terminated by different atomic columns and associated by stacking faults were reported in α-Al$_2$O$_3$ based on bright-field STEM imaging technique[26], but later considered by Lagerlöf et al. as questionable[27]. Heuer et al. did similar experiments[28], using the negative spherical aberration imaging technique combined with image simulations. It was found that the dislocation appeared to be stoichiometric and uncharged, and the dislocation cores exhibited 50% occupancy of the Al cations in order to achieve electrical neutrality. Thus, the determination of non-stoichiometric dislocation core is not straightforward, and further image simulation is necessary to verify the core stoichiometry. The models of the dislocation cores in this present study have been proposed according to the relative intensities of the atomic columns, and these intensities could be affected by the strain in the dislocation core. However, the stress fields of the edge-type dislocation cores should have no component along their dislocation lines[29]: there might be collective displacements of atomic columns in the plane with the dislocation end-on, but no misalignment within single atomic columns at the dislocation core. Thus, the overall intensities of the atomic columns at the dislocation cores of edge-type should not be
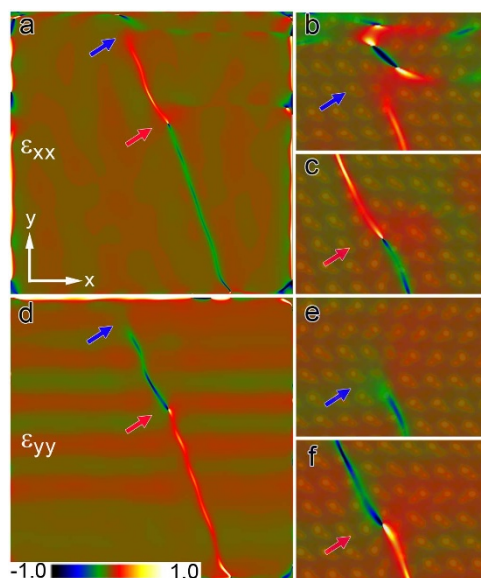
Figure 3 | Geometric phase analysis of the two dislocation cores with opposite ions. Geometric phase analysis based on the HAADF image obtained from the same area as Fig. 2(a) at lower magnification. The results of the normal strain components ε_{xx} and ε_{yy} are presented in (a) and (d), respectively. (b) and (c) ε_{xx} at core 1 and core 2 based on HAADF image at higher magnification. (e) and (f) ε_{yy} at core 1 and core 2, accordingly. The HAADF images are overlapped on (b), (c), (e), (f) to indicate the exact locations of the dislocation cores.

greatly affected by strain. Considering the large difference between the atomic number of In^{3+} (Z_{In} = 49) and As^{3-} (Z_{As} = 33), and the obvious intensity differences at the dislocation cores of the experimental image, it seems to be reasonable to determine the compositions of the single atomic columns in the dislocation cores in this way. Moreover, similar observations of unpaired Cd and Te atomic columns have recently been reported elsewhere[14].

Defects and associated long-range strain fields are of considerable importance in affecting the electronic properties of semiconductors, since the interaction of defects with charge carriers can occur far from defect cores[30]. Geometric phase analysis (GPA) is a method of obtaining local phase which can be directly related to any displacement field distorting the lattice fringes in the HREM image with respect to the reference lattice[31]. The corresponding strain field can then be found by analyzing the derivative of the displacement field. This method has been applied to the measurement of displacement fields around an edge dislocation in Si to an accuracy of 0.03 Å[32]. It is the lattice distortion that really matters in determining local displacement fields, and thus the GPA method is applicable to high resolution HAADF images once systematic lattice distortions from the microscope and CCD have been removed[33–34]. A GPA program compatible with Digital Micrograph was applied for calculation of the strain map around the dislocation cores, and the results of normal strain components along horizontal and vertical directions are presented in Figs. 3a and 3d, respectively. Except for the area including a stacking fault across the whole area of interest in one of the $(\bar{1}\bar{1}1)$ plane, both ε_{xx} and ε_{yy} are approximately zero, indicating extremely low levels of strain away from the $(\bar{1}\bar{1}1)$ stacking fault planes.

The blue and red arrows indicate the locations of core 1 and core 2. The strain component ε_{xx} changes from negative to positive passing across core 1; conversely, ε_{xx} changes from positive to negative passing across core 2, as presented in Fig. 3a. The variations of ε_{xx} across the dislocation cores obtained from an HAADF image recorded at higher magnification are shown with greater detail in Figs. 3b–3c; and the corresponding HAADF images are overlapped to indicate the exact locations of the dislocation cores. It appears that the
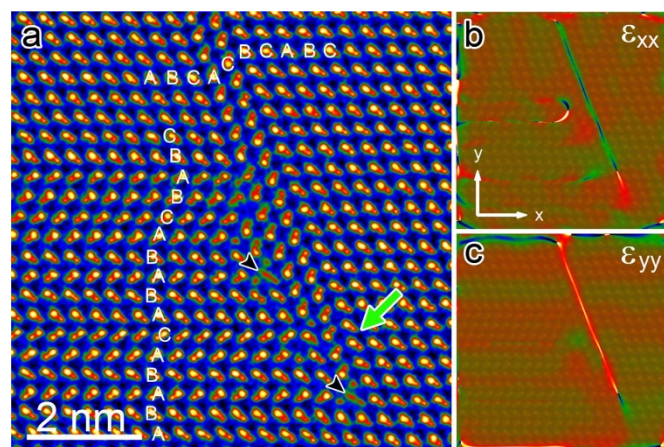

Figure 4 | Atomic structures and strain field distributions of the dislocation core at the bottom corner of the Z-shape faulted dipole. (a) Aberration-corrected HAADF image of dislocation core 3 as indicated by green arrows in Figs. 1(b) and (c). The stacking sequences are overlapped, and some of the ambiguous atomic arrangements are pointed out by black arrow heads. (b) and (c) Strain components of ε_{xx} and ε_{yy} based on geometric phase analysis of the overlapped HAADF image, which includes the core area shown in (a).

dislocation cores are source of strain inversion, whereas the stacking faults maintain the existing strain status until the next dislocation core is encountered. The strain component ε_{yy} has similar features of strain variation across the dislocation cores, as presented in Figs. 3d–3f. The only exception is that ε_{yy} for core 1 (Fig. 3e) has no contrast above the core where the lattice spacing along the y direction is not disturbed by the dislocation or the stacking fault below. These results appear reasonable in that the edge dislocation has compressive strain (negative) on the side of the slip plane with the extra half plane, and tensile strain (positive) on the other side, while the stacking fault has collective displacements parallel to the stacking fault plane, and thus has the same strain status. The reversed variations of strain fields for core 1 and core 2 reflect the different types of core structures presented in Fig. 2.

Fig. 4a is an aberration-corrected HAADF image of the area indicated by the green arrow in Figs. 1b–1c, which is formed by interactions of a stacking fault in the $(\bar{1}\bar{1}1)$ plane with multiple stacking faults in (111) planes. There are also single atomic columns in this area, and some image features not clearly resolved which could be due to local thickness changes. Stacking sequence analysis was carried out and overlapped on the image, and the overall Burgers vector $\mathbf{b}_3$ was obtained by adding up all of the displacement vectors around the area including multiple dislocation cores: $\mathbf{b}_3 = (1/3)[2\bar{7}3]$, or projected Burgers vector of $\mathbf{b}_{3\text{-proj}} = (1/6)\,[\bar{5}\bar{5}6]$ in $(\bar{1}10)$ plane. GPA analysis is also carried out in this area, and the results of strain components ε_{xx} and ε_{yy} are presented in Figs. 4b–4c. ε_{xx} remains negative along the stacking fault parallel to the $(\bar{1}\bar{1}1)$ plane, which is consistent with the lower part of Fig. 3a since there are no dislocation cores between them. The negative ε_{xx} changes to positive close to the bottom end of the stacking fault which might be considered as the equivalent dislocation core of the whole area. The strain component ε_{yy} shows similar features of strain variations along the $(\bar{1}\bar{1}1)$ stacking fault plane.

Discussion

Overall, our results have demonstrated that aberration-corrected HAADF imaging is a very powerful technique for determining atomic arrangements in and around dislocation cores. This approach has allowed us to distinguish between two types of dislocation cores which are part of a Z-shape faulted dipole, and variations of bond

lengths at the dislocation core are clearly resolved. Subsequent GPA analysis of the same area provides confirmation that the dislocation core serves as the origin of strain field inversion whereas the stacking fault acts to retain the existing strain. This combination of atomic structural information and strain distribution can be used as a starting point for studies of electronic properties of such defects within semiconductors, and these techniques should likewise be applicable to other types of defects in nanocrystals.

Methods

The InAs nanopillars, with nominal Sb concentration of 10%, were grown on nanopatterned substrates by metal-organic chemical vapor deposition in the catalyst-free growth mode (Detailed growth information will be published elsewhere). The nanopillars were deposited on copper grids with carbon support films for electron microscopy observation. Conventional transmission electron microscopy (TEM) and high resolution electron microscopy (HREM) were carried out using a Philips CM200-FEG transmission electron microscope. The aberration-corrected HAADF observations were performed using a JEOL ARM200F TEM (camera length: 6 cm, convergence angle: 20 mrad, collection angle: 90~170 mrad). All microscopes were operated at an accelerating voltage of 200 kV.

1. Algra, R. E. *et al*. Twinning superlattices in indium phosphide nanowires. *Nature* **456**, 369–372 (2008).
2. Caroff, P. *et al*. Controlled polytypic and twin-plane superlattices in III-V nanowires. *Nat. Nanotechnol.* **4**, 50–55 (2009).
3. Dick, K. A., Thelander, C., Samuelson, L. & Caroff, P. Crystal phase engineering in single InAs nanowires. *Nano Lett.* **10**, 3494–3499 (2010).
4. Xu, T. *et al*. Faceting, composition and crystal phase evolution in III-V antimonide nanowire heterostructures revealed by combining microscopy techniques. *Nanotechnology* **23**, 095702 (2012).
5. Akopian, N., Patriarche, G., Liu, L., Harmand, J. & Zwiller, V. Crystal phase quantum dots. *Nano Lett.* **10**, 1198–1201 (2010).
6. Spirkoska, D. *et al*. Structural and optical properties of high quality zinc-blende/wurtzite GaAs nanowire heterostructures. *Phys. Rev. B* **80**, 245325 (2009).
7. Li, L. *et al*. Polarization-induced charge distribution at homogeneous zincblende/wurtzite heterostructural junctions in ZnSe nanobelts. *Adv. Mater.* **24**, 1328–1332 (2012).
8. Dayeh, S. A., Susac, D., Kavanagh, K. L., Yu, E. T. & Wang, D. Structural and room-temperature transport properties of zinc blende and wurtzite InAs nanowires. *Adv. Funct. Mater.* **19**, 2102–2108 (2009).
9. Gottschalk, H., Patzer, G. & Alexander, H. Stacking fault energy and iconicity of cubic III-V compounds. *phys. stat. sol. (a)* **45**, 207–217 (1978).
10. Xu, X. *et al*. Distortion and segregation in a dislocation core region at atomic resolution. *Phys. Rev. Lett.* **95**, 145501 (2005).
11. Chung, S., Choi, S., Yamamoto, T. & Ikuhara, Y. Atomic-scale visualization of antisite defects in LiFePO$_4$. *Phys. Rev. Lett.* **100**, 125502 (2008).
12. Krivanek, O. L. *et al*. Atom-by-atom structural and chemical analysis by annular dark-field electron microscopy. *Nature* **464**, 571–574 (2010).
13. Chu, M., Liou, S., Chang, C., Choa, F. & Chen. C. Emergent chemical mapping at atomic-column resolution by energy-dispersive X-ray spectroscopy in an aberration-corrected electron microscope. *Phys. Rev. Lett.* **104**, 196101 (2010).
14. Li, C. *et al*. From atomic structure to photovoltaic properties in CdTe solar cells. *Ultramicroscopy* **134**, 113–125 (2013).
15. Mader, S. *Electron Microscopy and Strength of Crystals* (Inter-science, New York, 1963).
16. Hirsch, P. B. *The Relation between Structure and Mechanical Properties of Metals* (H.M.S.O, London, 1963).
17. Seeger, A. & Wobser, G. Stacking fault dipoles in the face-centered cubic metals. *phys. stat. sol.* **18**, 189–206 (1966).
18. Carter, C. B. & Holmes, S. M. The study of faulted dipoles in copper using weak-beam electron microscopy. *Phil. Mag.* **32**, 599–614 (1975).
19. Spence, J. C. H. & Kolar, H. Lattice imaging of faulted dipoles in silicon. *Phil. Mag. A* **39**, 59–63 (1979).
20. Lim, S., Shindo, D., Yonenaga, I., Brown, P. D. & Humphreys, C. J. Atomic arrangement of a Z-shape faulted dipole within deformed GaAs. *Phys. Rev. Lett.* **81**, 5350–5353 (1998).
21. Rečnik, A., Möbus, G. & Šturm, S. Image-warp: a real-space restoration method for high-resolution STEM images using quantitative HRTEM analysis. *Ultramicroscopy* **103**, 285–301 (2005).
22. Jones, L. & Nellist, P. D. Identifying and correcting scan noise and drift in the scanning transmission electron microscope. *Microsc. Microanal.* **19**, 1050–1060 (2013).
23. Hartel, P., Rose, H. & Dinges, C. Conditions and reasons for incoherent imaging in STEM. *Ultramicroscopy* **63**, 93–114 (1996).
24. Delclos, S., Dorignac, D., Phillipp, F., Moulin, S. & Bonnot, A. M. UHREM investigation of stacking fault interactions in the CVD diamond structure. *Diamond Relat. Mater.* **8**, 682–687 (1999).
25. Yamakov, V., Wolf, D., Phillpot, S. R. & Gleiter, H. Dislocation-dislocation and dislocation-twin reactions in nanocrystalline Al by molecular dynamics simulation. *Acta Mater.* **51**, 4135–4147 (2003).
26. Shibata, N. *et al*. Nonstoichometric dislocation cores in α-alumina. *Science* **316**, 82–85 (2007).
27. Lagerlöf, K. P. D., Castaing, J. & Heuer, A. H. Do moving basal dislocations in sapphire (α-Al$_2$O$_3$) have non-stoichiometric cores? *Phil. Mag.* **89**, 489–499 (2009).
28. Heuer, A., Jia, C. & Lagerlöf, K. The core structure of basal dislocations in deformed sapphire (α-Al$_2$O$_3$). *Science* **330**, 1227–1231 (2010).
29. Hull, D. & Bacon, D. J. *Introduction to Dislocations* (Elsvier Ltd., Oxford, 2011).
30. Alexander, H. & Teichler, H. *Handbook of Semiconductor Technology* (Wiley-VCH, Berlin, 2000).
31. Hÿtch, M. J., Hÿtch, M. J., Snoeck, E. & Kilaas, R. Quantitative measurement of displacement and strain fields from HREM micrographs. *Ultramicroscopy* **74**, 131–146 (1998).
32. Hÿtch, M. J., Putaux, J. & Pénisson, J. Measurement of the displacement field of dislocations to 0.03Å by electron microscopy. *Nature* **423**, 270–273 (2003).
33. Lubk, A. *et al*. Evidence of sharp and diffuse domain walls in BiFeO$_3$ by means of unit-cell-wise strain and polarization maps obtained with high resolution scanning transmission electron microscopy. *Phys. Rev. Lett.* **109**, 047601 (2012).
34. Rossell, M. *et al*. Atomic structure of highly strained BiFeO3 thin films. *Phys. Rev. Lett.* **108**, 047601 (2012).

Author contributions

L.L. carried out the TEM experiments and wrote the paper, H.L. and H.Y. assisted the material growth, L.L., J.W. and D.S. designed the experiment. L.L., Z.G., M.M., H.Y., Y.G., J.W. and D.S. contributed to the data analyses and paper revisions.

Additional information

Supplementary information accompanies this paper at http://www.nature.com/scientificreports

Competing financial interests: The authors declare no competing financial interests.

How to cite this article: Li, L.Y. *et al*. Atomic configurations at InAs partial dislocation cores associated with Z-shape faulted dipoles. *Sci. Rep.* **3**, 3229; DOI:10.1038/srep03229 (2013).